Barotropic Trends through the Barents Sea Opening for the Period 1975-2021

Vahidreza Jahanmard[1], Ulrike Löptien[2], Anne Britt Sandø[3,4], Andrea M. U. Gierisch[5], Heiner Dietze[2,7], Vidar Lien [3,4], Nicole Delpeche-Ellmann[6], and Robinson Hordoir[3,4]

[1]Department of Civil Engineering and Architecture, Tallinn University of Technology, Estonia
[2]University of Kiel, Germany
[3]Institute of Marine Research, Bergen, Norway
[4]Bjerknes Centre for Climate Research, Bergen, Norway
[5]Danish Meteorological Institute, Copenhagen, Denmark
[6]Department of Cybernetics, Tallinn University of Technology, Estonia
[7]King's College London, UK

Key Points:

- A model of the Atlantic and Arctic Oceans simulates an increase of more than 20% for the Barents Sea Opening flow for the period 1975-2021
- Deep learning techniques link this increase to wind forcing over the Nordic Seas
- Changes of leading atmospheric modes over the North Atlantic and the Arctic apparently fail to explain the increases

Corresponding author: Robinson Hordoir, `robinson.hordoir@hi.no`

Abstract

We analyze the output of a regional ocean model that comprises the North Atlantic and the Arctic Ocean for the period 1975-2021. We focus on the flow through the cross-sections closing the Nordic Sea basin. The simulated flow at Barents Sea Opening (BSO) shows a clear positive trend. To understand the origin of this trend, we reconstruct the BSO flow based on wind time series over the Nordic Seas using Deep Learning. To explore potential links between the results from this reconstruction and the major atmospheric modes, we perform a suite of idealized experiments where the ocean model is forced with wind field anomalies that refer to known changes in the leading modes of atmospheric circulation over the North Atlantic and Arctic Oceans. Known changes in the major atmospheric wind patterns over the North Atlantic have a weak impact on the simulated BSO flow, and the sign is not consistent with the overall trend of the full simulation. The latter holds as well for the known temporal changes in the intensity of the Arctic Dipole mode. The weak temporal changes in the Arctic Oscillation are consistent with the trend in the BSO flow but could not explain its amplitude. Ultimately, we could not establish a clear link between the BSO flow trend and changes in the major atmospheric modes. We conclude that the atmospheric pattern responsible for the BSO flow trend, does not project directly on the leading modes of atmospheric variability over the North Atlantic and the Arctic.

Plain Language Summary

The Barents Sea Opening is an important gate between the Nordic Seas, that transports heat and salt towards the Arctic Ocean. The analysis of an ocean model shows that the simulated volume transport at the Barents Sea Opening increases for the period 1975-2021. Here, we set out to understand the origin of this trend. Guided by artificial intelligence we find a link between the trend and wind patterns over the Nordic Seas. In subsequent analyses we test for the effects of the most dominant atmospheric patterns over the North Atlantic and the Arctic. Our results suggest that the changes of the most dominant patterns fail to explain the trend in transports through the Barents Sea opening. We conclude that the trend is, rather, associated to more complex and specific atmospheric conditions.

1 Introduction

The Arctic Ocean is among the most vulnerable regions of the world that is strongly affected by climate change, e.g. by declining sea ice and glaciers. Part of the heat exchange between the sub-Arctic and Arctic occurs through the transport of relatively warm and saline Atlantic waters northward through the Nordic and Barents Seas to the Arctic Ocean. The Atlantic Water enters the Polar Basin through two main gateways: (1) through the Fram Strait between Greenland and the Svalbard archipelago and, (2) through the Barents Sea between mainland Norway and Svalbard. To-date, increased heat transport, carried by the Atlantic Water flow through the Barents Sea, is already causing profound changes to the Barents Sea marine environment (Lind et al., 2018), sea-ice cover (Onarheim et al., 2015; Yang et al., 2016) and marine ecosystem (Fossheim et al., 2015). As such, the Barents Sea appears to be an essential passage way for the transport of heat, both for the atmosphere and the ocean (Smedsrud et al., 2013). Since changes that occur in the Barents Sea are eventually also reflected in the Arctic Ocean, it is important to quantify and fully understand the different pathways of waters, the drivers behind them and their associated characteristics.

The exchanges through the southwestern entrance to the Barents Sea consists of a predominantly eastward flow in the southern and central parts (i.e. an inflow to the Barents Sea from the Nordic Seas) (R. Ingvaldsen et al., 2002; Skagseth et al., 2011) and a predominantly westward flow in the northernmost, deeper part (i.e. an outflow from the Barents Sea to the Nordic Seas) (Skagseth, 2008). The inflow into the southern and central Barents Sea Opening (BSO hereafter) is mainly barotropic (R. B. Ingvaldsen et al., 2004) and has been shown to be sensitive to local atmospheric forcing (R. Ingvaldsen, 2005). The outflow out of the northern part of the BSO is dominated by a baroclinic component (Blindheim, 1989) from dense water formation due to sea-ice formation in western parts of the Barents Sea (Blindheim, 1989; Sarynina, 1969; Årthun et al., 2011), but has also been shown to be sensitive to atmospheric forcing with intermittent reversals (Lien et al., 2013).

From a barotropic viewpoint, the cause of temporal changes and trends in the Atlantic Water flow through the Barents Sea may be simplified down to two hypotheses based on hydraulic principles: either changes in upstream conditions push water into the Barents Sea, or changes in downstream conditions pull water into the Barents Sea (or both). Upstream changes in the Atlantic Water flow can be caused by processes in the North Atlantic that cause increased inflow to the Nordic Seas through the gateways between Scotland and Iceland (Figure 1), or wind-driven changes to the circulation within the Nordic Seas. Changes in the downstream conditions include wind-driven changes to the inflow at the southwestern entrance to the Barents Sea (R. B. Ingvaldsen et al., 2004; Skagseth et al., 2011; Lien et al., 2013, 2017) as well as changes in dense water formation within the Barents Sea affecting the strongly baroclinic outflow to the northeast toward the Polar Basin (Midttun, 1985; Schauer et al., 2002; Dmitrenko et al., 2015). From a more general point of view, the gates towards the Arctic Ocean and the Nordic Sea basin are interconnected, and any change in a flow of a gate drives a change in another, but the notion of causality is unclear on which gate drives which (de Boer et al., 2018): such a notion is linked to high frequency signal as barotropic waves may travel from one gate to another in a few hours or less.

It has been postulated that changes in the downstream conditions may also cause feedback loops that will tend to further strengthen the response in the Atlantic Water inflow to the Barents Sea (Ådlandsvik & Loeng, 1991; Bengtsson et al., 2004). Two feedback loops, one atmospheric and one oceanic, were investigated by Smedsrud et al. (2013). They found that increased dense water formation that increases the baroclinic flow from the Barents Sea to the Polar Basin also tends to increase the inflow to the Barents Sea in the southwest. However, the other feedback loop, where reduced sea-ice cover from increased Atlantic Water inflow causes increased ocean-to-atmosphere heat fluxes and subsequently increased cyclonic circulation in the atmosphere that favors increased inflow in the southwest, was not substantiated.
Polyakov et al. (2023) related recently, in an empirical study, the BSO flow trend, to one of the leading atmospheric modes over the Arctic Ocean, the Arctic Dipole (AD). In contrast, Hilmer and Jung (2000) refer to circulation changes in the Nordic Seas due to changes in the centers of action in the North Atlantic Oscillation.

There is, however, no consensus yet on the drivers of the flow trend at BSO. In the present study, we add to the ongoing discussion on the origin of the flow trend. Since the BSO flow in general has been shown to be sensitive to wind patterns over the Nordic Seas (Muilwijk et al., 2019; Chafik et al., 2015), we hypothesize that the flow trend at BSO is linked with a change in wind patterns over the Nordic Seas. Such a change is noticed by Herbaut et al. (2017) for example, although their findings conclude to a weakening of the cyclonic circulation in the Nordic Seas, which according to Muilwijk et al. (2019) should also weaken the flow towards the Barents Sea at BSO, and can therefore not explain the BSO flow trend. To explore our hypothesis, we utilize results from an ocean general circulation model for the period 1975-2021. More specifically, we explore links between the simulated trend in the Atlantic Water flow through BSO and its drivers using deep learning (DL hereafter). Technically, we use output from our geophysical fluid dynamic model as inputs to a deep-learning model. The approach sets out to find a set of features (such as atmospheric times series) that yield explanatory power in terms of reproducing the flow through BSO. The application of Deep learning is embedded in a range of respective recent oceanographic advances, including data assimilation, improvements of hydrodynamic models, forecasting, and gap filling (Brajard et al., 2020; Rajabi-Kiasari et al., 2023; Jahanmard et al., 2023; Dietze & Löptien, 2021).

In Jahanmard et al. (2023) a temporal causal convolutional network was employed to predict ocean modelling errors given particular input variables. This approach basically examines the frequency contents of ocean modelling errors and searches for causal relationships between ocean model errors and input variables, with the requirement that the DL model must generalize its solution across different unseen sets. The advantage of this approach is the distinct identification of relevant input variables and their characteristics. Here, we will use a similar approach (see Section 3) to analyze the model outputs and relate it to specific wind derived time series (chosen based on expert knowledge). The aim is to perform a non-linear Granger causality test (Gogina & Zettler, 1999; Diebold, 2007) for determining whether the simulated BSO flow and its trend can be successfully reconstructed by using the wind time series only. In a second step, we attempt to identify the most influential time series by feature selection. Our specific DL approach additionally allows us to determine the memory of the system by using so called *causal convolutions.*

The DL experiments are complemented with sensitivity experiments with our ocean model to explore the role of wind changes that refer to known changes in the dominant atmospheric modes over the Arctic.

The paper is organized as follows: we start with a description of our physical ocean modelling experiment in Section 2. In section 3, we present our DL approach to reconstruct the BSO flow and respective physical implications. In Section 4, we employ the results of the DL-based model experiments, to design a set of sensitivity experiments with the prognostic general ocean circulation model targeted to identify the atmospheric drivers behind the flow trend at BSO. Section 5 discusses our findings and concludes this article.

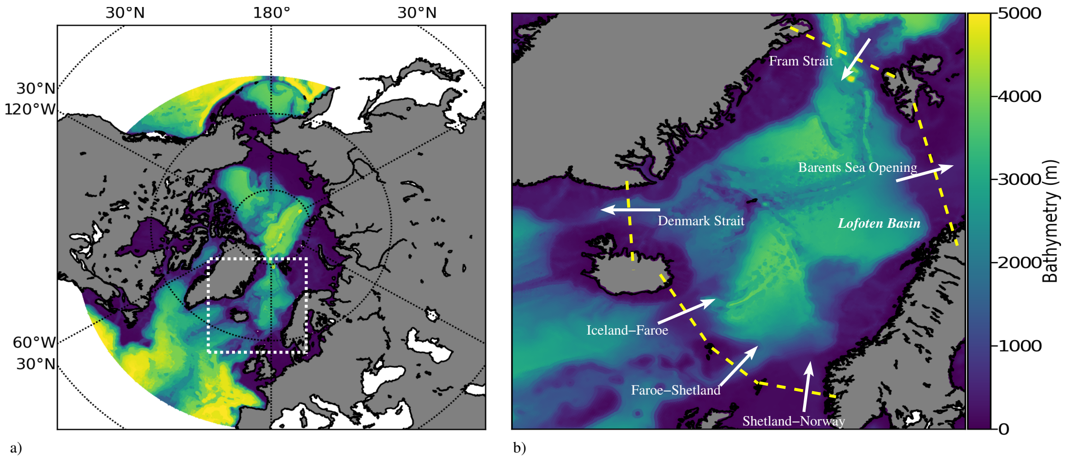

Figure 1. a) Domain and bathymetry (in m) of the Nemo-NAA10km model configuration, the white square shows the box covering the Nordic Seas b) The Nordic Sea box, with its 6 gates, Barents Sea Opening (BSO hereafter), Fram Strait (Fram hereafter), Denmark Strait (DS hereafter), Iceland-Faroe ridge (IF hereafter), Faroe-Shetland Channel (FS hereafter) and Shetland-Norway section (SN hereafter). The direction of the arrows shows the direction of the mean flow at each gate.

2 General Ocean Circulation Model, Transport Trends & Dataset Description

We use a long term simulation of the Nemo-NAA10km regional ocean model (Hordoir et al., 2022) for the period 1975-2021. Nemo-NAA10km is a regional model used to study ocean processes, and changes in ocean processes in the North Atlantic and Arctic Oceans. Nemo-NAA10km operates in forced mode (as opposed to ocean-atmosphere coupling). The interaction with atmospheric data is parameterized through bulk formulas (Large & Yeager, 2004). The wind stress received by the ocean is calculated as a function of the square of (prescribed) winds in 10 m height. The effects of surface currents on wind stresses are neglected. The latter facilitates the interpretation of the effect of wind-patterns on circulation because there is no feedback from potentially chaotic differences in the circulation.

Within the computational domain of Nemo-NAA10km that covers the Arctic & North Atlantic Oceans (Figure 1a), we define a box that covers the Nordic Seas (Figure 1b), and for which each of the 6 gates to the Nordic Seas is described.

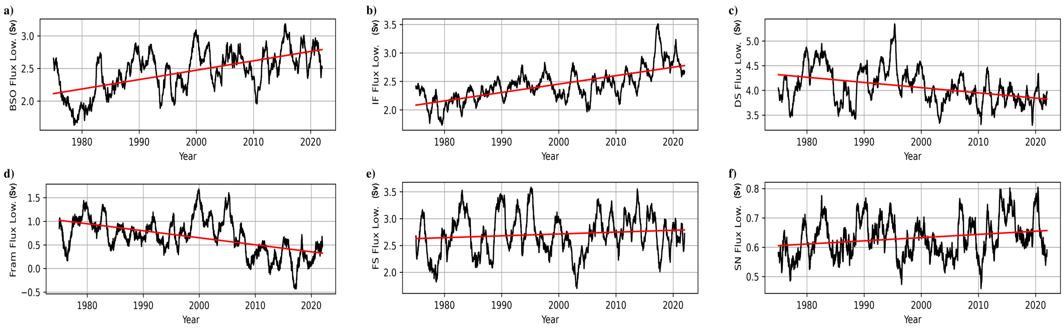

Figure 2. Low passed filtered net flow (in Sv) at the 6 different gates of Figure 1 for the time period 1975-2021, the figures show the annual mean signal computed with a moving average, and the linear trend for the entire time period (red line). All fluxes have a positive mean value, but their contribution to the budget of the Nordic Sea box is indicated hereafter with a (+) or (-) sign. a) BSO (-), linear trend of +0.15 Sv per decade b) IF (+), linear trend of +0.14 Sv per decade c) DS (-), linear trend of -0.11 Sv per decade d) Fram (+), linear trend of -0.15 Sv per decade e) FS (+), linear trend of +0.03 Sv per decade f) SN (+), linear trend of +0.01 Sv per decade.

We focus on the barotropic variability within the Nordic Seas box defined in Figure 1. We compute the barotropic volume flux through each of the gates for the period 1975-2021, and the computation is done hourly. There is an obvious trend of net transport at BSO leaving the Nordic Sea box. The Nordic Sea box budget is mostly compensated by a stronger input to the Nordic Sea box at the IF ridge, and a decreasing southward trend at DS (Figure 2). Additionally, the southward flow at Fram declines. These calculations suggest a change in the transport in the Nordic Sea. This is also reflected in changes of the barotropic circulation for two different periods (Figure 3), which shows also that the flow along the Norwegian coast actually becomes less. Along the coast of Greenland, the southward flow intensifies, but the northward inflow at DS becomes higher, resulting in a weaker net southward flow. The fate of the increasing flow at BSO is not investigated in the present article. It is possible that the flux through Bering Strait, or through the Canadian Archipelago is modified. In the latest case, the Southward flow at Davis Strait is estimated to be 2.6 Sv (Cuny et al., 2005), which is of the same order of magnitude as that of the BSO. The flow through this strait could therefore increase by the same amount as the BSO flux.

This study sets out to link trends in transports to wind forcing. We start with employing DL to explore statistical relationships. In a subsequent step (4.2) we go back to the prognostic general ocean circulation model in order to test the results and hypothesis suggested by the results of the Deep Learning.

The data supplied to the DL pipeline consists of several wind features for the entire or a sub-section only of the area of the Nordic Sea domain (Figure 1). These wind features are the mean zonal wind stress τ_x, the meridional wind stress τ_y, and the vertically integrated Sverdrup transport V in m^2 s^{-1} (Gill, 1982):

$$V = \frac{1}{\beta\rho_0}\left(\frac{\partial\tau_y}{\partial x} - \frac{\partial\tau_x}{\partial y}\right) \tag{1}$$

in which

$$\beta = \frac{2\omega cos(\phi)}{R} \tag{2}$$

where $\omega = 7.2110^{-5}$ s^{-1} is the earth rotation pulsation, ϕ is the latitude, and R is the earth radius. It is important to note that this Sverdrup transport is a theoretical equation which only permits to isolate a single process that must be reproduced by Nemo-NAA10km. The spatially averaged values of τ_x, τ_y and V are computed for several sub-areas of the Nordic Sea box. In total, these areas comprise the entire Nordic Sea box itself, the 500m isobath along the Norwegian coast (i.e.: the pathway of the Norwegian current transporting Atlantic Water towards the BSO), the Lofoten Basin, FS, DS, IF, Fram, SN, and BSO itself (Figure 4). The 500m isobath is transformed into an area by considering all the model grid cells with a depth of 500m $\pm$ 10m.

The features provided for the reconstruction of the BSO flow at a given hour, are either from the same hour, or from previous hours. It is important to notice that the effect of τ_x & τ_y features on ocean circulation have a different timescale than the Sverdrup transport V. The reason is that, implicitly, a steady state assumption of different physical processes (each of which with its own dynamics) is made: τ_x & τ_y can be related with the Ekman transport in the ocean (Gill, 1982), for time scales $t \gg \frac{1}{f}$, in which f is the local Coriolis parameter. For the Nordic Seas area, $\frac{1}{f}$ it is approximately 2 to 3 hours. The timescale above which a steady state can be considered when it comes to the Sverdrup transport V is different, and is related with the size of the basin (Willebrand et al., 1980). This timescale T can be computed as:

$$T = \frac{L}{\beta}\left[\frac{1}{L^2} + \frac{f^2}{gH}\right] \tag{3}$$

in which L is a scale of the width of the basin, H is a scale of the depth of the basin, $g = 9.8m^2s^{-1}$. Applied to the Nordic Seas, we compute T to be equal to 2 to 3 days, which means that a timescale much larger than that of the basin timescale is of the order of a few weeks. Computing V will therefore require considering time scales of a larger amplitude than T (Willebrand et al., 1980). Results from the DL model will show in the present article, that the reconstruction of the long term trend at BSO requires a learning process with a data time slot that corresponds to such time scales.

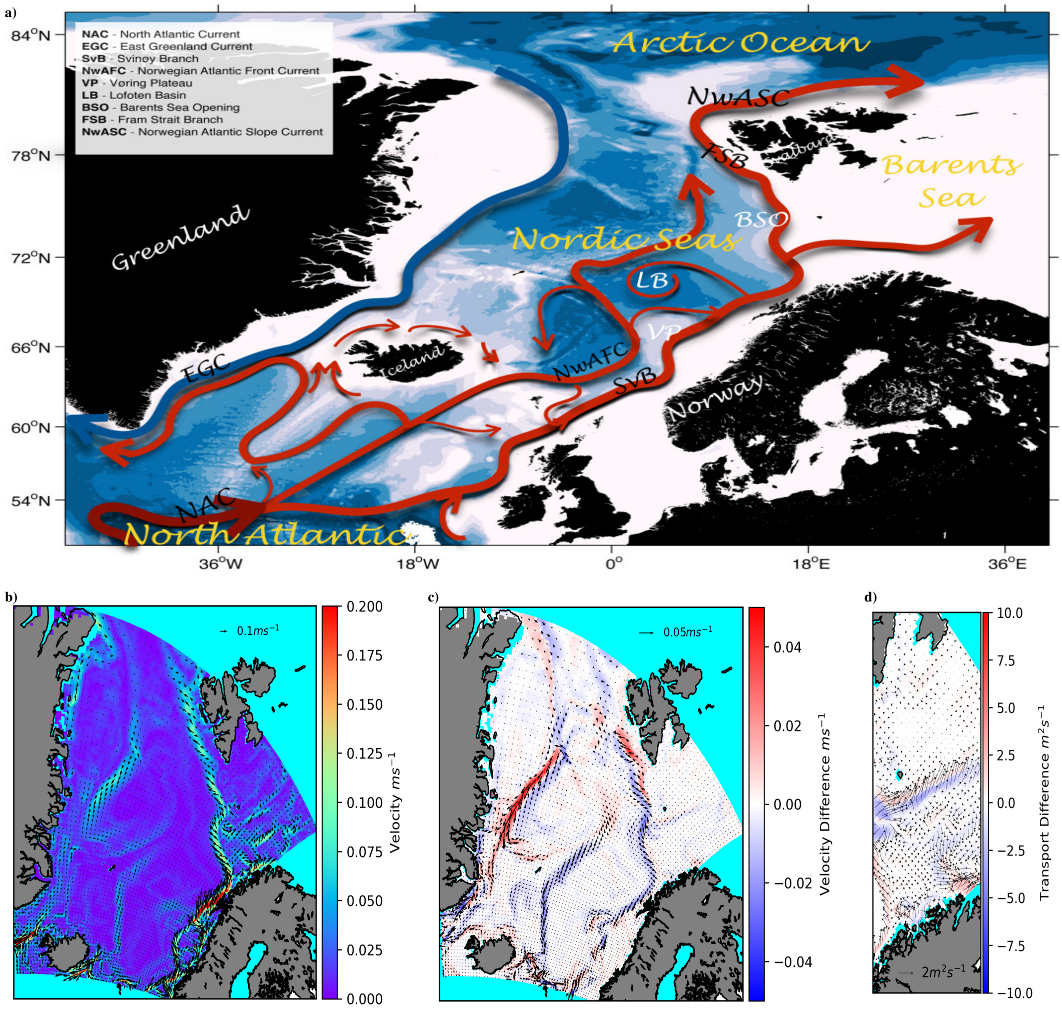

Figure 3. a) From Chafik et al. (2015), Map of the Nordic Seas including the bathymetry (shading) and a schematic representation of the large-scale pathways of Atlantic water in the northern North Atlantic and the Nordic Seas. Abbreviations in black denote current systems, and white denote regions. The focus of the present study is the variability of the branch entering the Barents Sea at BSO. Subfigures b,c and d show current patterns extracted from the Nemo-NAA10km numerical configuration (Hordoir et al., 2022). (b) Mean barotropic currents in m s^{-1} for the period 1992-2006 c) Difference between the periods (2007-2021 - 1992-2006) d) Difference of transport in m^2 s^{-1} at BSO, between the periods (2007-2021 - 1992-2006)

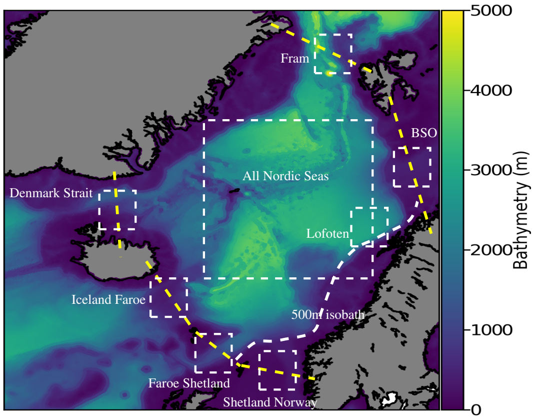

Figure 4. Boxes over which we compute mean hourly values of τ_x, τ_y and V, that are provided as input to our DL model. The dotted-dashed line shows the 500m isobath along the Norwegian coast.

3 Deep Learning Method

In this section, we present a reconstruction of the temporal evolution of the BSO flow based on local timeseries of surface winds using a multivariate deep neural network. Guided by expert knowledge we find a suite of local wind time series (cf. Figure 4) that suffice to reconstruct the BSO flow. The DL model architecture employed is a temporal causal convolutional network. In our benchmarking, we observed that the final architecture exhibits a smaller generalization error and demonstrates better performance in capturing both high- and low-frequency variations than test experiments described below. This architecture is capable of establishing complex relationships between the past temporal evolution of the wind derived time series (as a receptive field RF) and the simulated BSO flow while preventing information leakage from future to past. How many past information are used can be adjusted as the network uses *causal convolutions* which are just convolutions that make sure that the prediction at time t only depends on past events t - n, where n is the length of RF. In a nutshell, we can explore whether the past evolution of the wind time series is useful to forecast the BSO flux variations and its trend (non-linear Granger causality test) and additionally determine the memory of the system (by varying RF). Ultimate conclusions are then drawn by combining the DL results with physical considerations. Details on the DL model architecture are described in Appendix A.

The ultimate network is based on expert knowledge combined with a couple of DL experiments. Specifically, we tested different subsets of input variables to explain the model's outcome (following a similar approach as J. Chen et al. (2018)). For instance, we included flows from other gates (see Figure 1b) into the models inputs. These results, however, were inconclusive and did not improve the quality of the reconstruction. In this case, physical constrains limit the RF to 2 or 3 hours (which is bouncing time occurs at the speed of barotropic waves). An event that happened at other gates must precede an event in the BSO gate to be considered in our DL experiments. Therefore, if we want to consider the flows, the RF had to be limited to a few hours. Our experiment demonstrated that including these flows did not improve the quality of the reconstruction. Excluding the flows of other gates and expanding the RF time, the model strongly improved in predicting the trend. Additional experiments revealed that an hourly resolution of the input data results in an improved model performance compared to a daily resolution. Our final DL model achieves a correlation R^2 of 0.97, and a reproduction of the trend with a trend ratio TR of 0.92 in predicting the BSO flow.

To determine the memory of the system, Figure 5 shows the evolution of TR and R^2 as a function of RF. This figure indicates that using three weeks of historical wind-derived time series allows for retrieving the BSO trend. Choosing an RF greater than three weeks does not impact the model's performance in reconstructing the BSO trend.

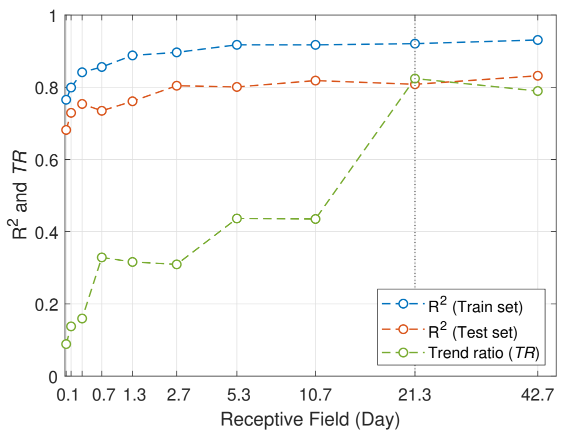

Figure 5. Evolution of the BSO trend ratio (TR) and model performance (R^2) as functions of the receptive field (RF).

4 Synthesis

4.1 Deep Learning Results

For the hourly BSO flow reconstruction we use hourly wind indexes representative of areas as indicated in Figure 4 backlogged up to three weeks. By combining expert knowledge with trial-and-error we find that in order to reconstruct the flow: (1) All wind data backlogged as far as 21 days and, occasionally, even as far back as 30 days is required. (2) Daily resolution is insufficient, as it fails to capture the full amplitude of the trend in BSO flow (Figure 2). Hence, we use hourly wind data and then reconstruct hourly BSO flow. Through probing through various input combinations to our deep learning framework in order to reconstruct the BSO flow as simulated with our prognostic general ocean circulation model, we find indications that:

- The long-term trend of the barotropic BSO flow is wind driven. The reason being that a precise reconstruction can be achieved by using hourly winds. Note that the effect of model boundary conditions on the BSO flow trend is apparently minor because: (1) The models open boundary conditions are based on monthly mean values, and we found that shorter than daily frequencies are required to reconstruct the trend. (2) Barotropic waves protruding from the boundaries of the Nordic Seas are created by weather systems which cannot yet have reached the Nordic Seas. Given that BSO flow can be reconstructed using past data only, this suggests that there is a temporal fallacy in the argument that the models boundary conditions drive the BSO flow trend.
- The BSO flow long term trend is pushed by wind patterns over the Nordic Seas, but the "pull" hypothesis can not be totally excluded as weather systems over the Nordic Seas can move to the Barents Sea for example. And since they arrive in

the Barents Sea afterward, it is not impossible that their pattern in this area resembles that of the indexes we provide to the DL model.

- It is possible to reconstruct the BSO flow, and its trend, using data from sea-ice free regions. We can therefore conclude that sea-ice has little or no influence on the BSO flow.

Based on our results so far, we have identified that the trend observed from the BSO is most likely driven by a change in wind circulation over the Nordic Sea area. But the question remains, in terms of physical understanding, on how can we characterize this change. We continue to investigate this aspect by using Principal Component Analysis (Empirical Orthogonal Functions).

4.2 Atmospheric Patterns

We have shown that the long term trend at BSO is linked to winds. However, since the wind time series are statistically related we cannot draw ultimate cause-effect relationships on what are the specific changes in the atmospheric circulation that could explain such trends. Thus subsequent analysis refer to model simulations which are motivated by foregoing studies.

Based on work of R. B. Ingvaldsen et al. (2004) (their Figure 12) we know that there are two basic patterns driving BSO flow variability, one for each direction of the flow. In the case of an inflow from the Nordic Seas towards the Barents Sea, the flow is associated with a low pressure system centered on the Nordic Seas, which creates a cyclonic circulation in the Nordic Seas. In the case of an outflow from the Barents Sea, towards the Nordic Seas, the flow is associated with a high pressure system centered north of Greenland, which extends in the Nordic Seas. The prominent overall trend of increased BSO flow (Figure 2) can be decomposed in two sub-trends. The trend of inflows, and the trend of outflows. The trend of the total BSO flow is 1.5 10^4 m^3 s^{-1} per year, but the trend of inflows is actually 1.4 10^4 m^3 s^{-1} per year, whereas the trend of outflow is 7.38 10^4 m^3 s^{-1} per year.
In the present article, we are only considering the net flow through BSO, and BSO is defined as a section going from Svalbard to the Norwegian continental coast. However, the BSO flow is not homogenous along this section. It is mostly inflowing along the Norwegian coast, and can be outflowing South of the Island of Bjørnøya, which is also the deepest part of the section. If the trend of outflows can be related with the trend of the outflowing part of the BSO flow, and the trend of inflows can be related with that of the inflowing part of the BSO flow, then one can deduce that the outflows should become weaker and/or less frequent. A closer look at the trends in currents and transports shows that this is actually what happens in our numerical simulations (Figure 3c and 3d). This suggests that the wind pattern associated with outflows has a trend making it weaker, as the trend of outflow strength is more than 5 times higher. Of course, since outflows are rare in comparison with inflows, the total BSO flow trend is not just simply the algebraic sum of the two trends.
In our model experiments, we follow a similar approach as outlined by Muilwijk et al. (2019). We design a perturbation experiment in which the wind field of the forcing dataset of the long term simulation of Hordoir et al. (2022) is modified by adding constant wind fields. These wind fields correspond to the major atmospheric modes (North Atlantic Oscillation, East Atlantic Pattern, Arctic Oscillation and Arctic Dipole). Thus, our pattern differs from Muilwijk et al. (2019) who modified his forcing by an anomaly corresponding with a very strong or very weak sea level pressure (SLP) at the location of the low pressure system located in the Greenland Sea. Our analysis is motivated by earlier suggestions on the potential impact of changes in the leading atmospheric modes (Polyakov et al., 2023; R. B. Ingvaldsen et al., 2004)).

For this purpose, we perform Principal Component Analyses of sea level pressure (SLP) anomalies for the following regions: (1) the North Atlantic from 20°-80°N and 90°W-40°E and (2) the Arctic ranging from 20°-80°N, 180°W-180°E. All calculations are based on monthly mean SLP anomalies where the mean seasonal cycle was removed. The atmospheric data consist of the ERA5 reanalysis that was also used to force the model. Note that the data sets were not de-trended. The corresponding wind fields were obtained by regressing the indices on the respective wind fields over the Northern Hemisphere.

We considered two leading modes for both regions. For the first region, comprising the North Atlantic, we perform separated principal component analyses for the time periods 1979-1988 and 2013-2022. The rationale of this approach is to explore the impact of known changes in the centers of actions in the leading modes over time (Tao et al., 2023; Hilmer & Jung, 2000; Jung et al., 2003; Barnston & Livezey, 1987). The trends in the intensity of these leading modes over time are rather weak. For the Arctic, however, the Arctic Dipole has a tendency toward higher values over time. Also, this mode has been suggested to strongly impact the BSO flow in the empirical study by Polyakov et al. (2023). We thus performed the principal component analyses over the entire time period that is based on the ERA5 atmospheric conditions.

All respective wind anomalies (referring to the positive and negative EOF-patterns) were added to the regular wind forcing of the year 2000 (which is in approx. the middle of the simulated time period). Note that the original winds were rather weak to moderate when starting the simulations with modified forcing.

4.3 Leading modes in the North Atlantic: the North Atlantic Oscillation and East Atlantic Pattern

For the North Atlantic region, we explore how the known changes in the position of the centers of action in the leading modes of atmospheric variability might impact the simulated BSO flow. We compare the two time periods 1979-1988 and 2013-2022 for the first two leading modes, the North Atlantic Oscillation or NAO, and the East Atlantic Pattern-EA (Hurrell, 1995). Note that shifts in the NAO can result in related shifts in the EA pattern (Mellado-Cano et al., 2019). The time periods refer to the first and last decade during which we applied consistently ERA5 atmospheric forcing. For the NAO we compare the impact of positive and negative anomalies during the two periods because the response could be non-symmetrical. For the EA we consider only the positive phases because it knowingly developed a preference for more positive values during the recent decades (Mikhailova & Yurovsky, 2016).

Although there is a clear change in the location of the low pressure system centered on the Nordic Seas between the two time periods, especially if one considers the NAO, this change does not imply the expected increase at the BSO flow (Figure 6). On the contrary, the changes of wind strength between the two time periods, lowers the BSO flow, as the wind vorticity on the area shifts (Figure 6 a). This change is consistent with the changes of currents, which exhibit a weaker Atlantic Current (Figure 3). The other sensitivity experiments which apply the wind velocity changes related with the difference in EA produce almost no visible change in BSO flow. If the experiment is done based on the negative NAO phase, then the BSO flow does increase by about 2%, which is far below the 20% of increase represented by our Nemo-NAA10km simulation. Our results differ from the ones conducted by (Muilwijk et al., 2019) as the ocean response in our experiments is weaker, but the perturbation we introduced is much weaker as it corresponds to observed trends in leading modes over the North Atlantic. The pattern of change of NAO over the North Atlantic Ocean exhibits a trend towards a weaker low pressure system over the North Atlantic (Figure 6), which suggests that the cyclonic wind circulation becomes slightly weaker, hence creating a weaker cyclonic ocean circulation in the Nordic Seas. Based on the experiments made by (Muilwijk et al., 2019), one should

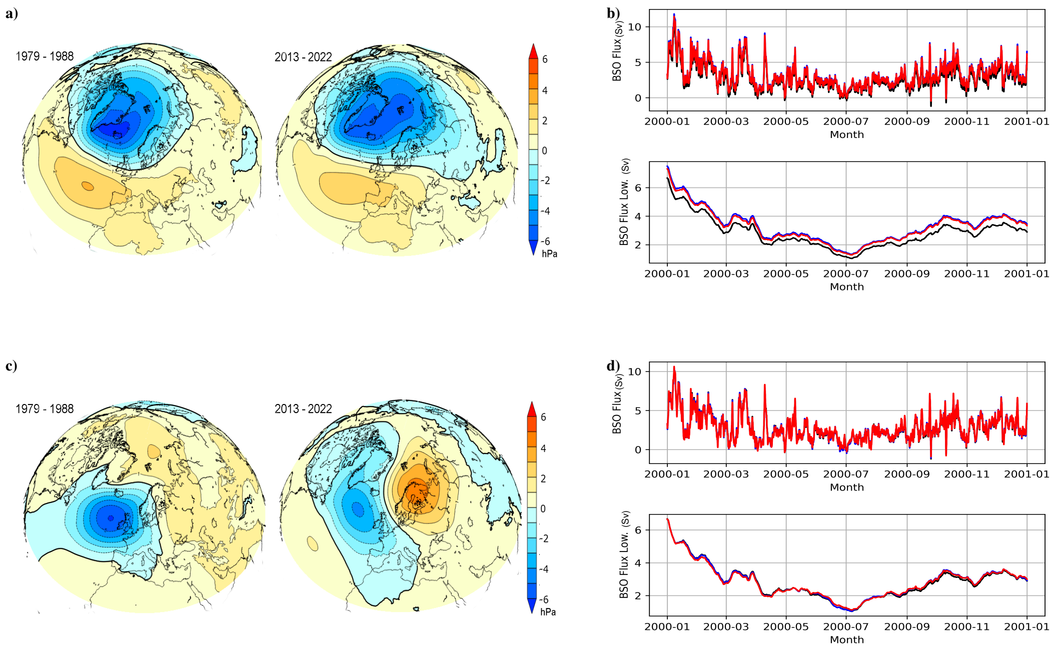

Figure 6. a) First EOF of the SLP (NAO) over the North Atlantic Ocean, for the time periods 1979-1988 and 2013-2022 b)Sensitivity of the BSO flow for year 2000 to an increased EOF1 pattern for the 1979-1988 and 2013-2022 time periods. Black curves are the reference experiment, blue curves correspond to the time period 1979-1988, red curves to the time period 2013-2022 instead. For each subfigure, the hourly signal is displayed above (BSO flow), and a low passed signal is displayed below (BSO flow Low.) c) Second EOF of the SLP (EA) over the North Atlantic Ocean, for the time periods 1979-1988 and 2013-2022 d) Sensitivity to an increased EOF2 pattern

expect the BSO flux to be a bit weaker for the period 2013-2022 compared with the period 1979-1988, which is exactly what our experiment shows. Therefore, we conclude that the trend of BSO flux can not be explained by the changes of principal atmospheric modes over the North Atlantic.

4.4 Leading modes over the Arctic: the Arctic Oscillation and Arctic Dipole

The Arctic Oscillation (AO hereafter) and the Arctic Dipole (AD hereafter) correspond to the two leading modes when considering the sea level pressure anomalies north of 70°N (Thompson & Wallace, 1998; Deser, 2000; Watanabe et al., 2006; Wu et al., 2006). In contrast to the NAO, the AO and AD are associated with outflows at BSO. We explore the first two leading modes while we do not consider a shift in the pattern but performed, instead, the EOF analysis for the entire period 1979-2022 (because the AO pattern is typically more stable than the NAO). We explore the impact of the related positive and negative anomalies in the winds. Such an approach allows us to estimate a potential impact of a trend or a phase shift in the leading modes. A respective phase shift has been reported for the AD (Heo et al., 2021).

In contrast to the experiments performed with the NAO and EA, the simulated BSO flow is extremely sensitive to the AD as suggested already by Polyakov et al. (2023); R. B. Ingvaldsen et al. (2004). Polyakov et al. (2023) related changes in the ORAS5 ocean reanalysis data to the trend in one of the leading atmospheric modes over the Arctic Ocean, the Arctic Dipole (AD). By time series analysis Polyakov et al. (2023) attribute the BSO flow trend to the increasing strength of the AD. Our model simulations could, however, not confirm this empirically drawn relationship. In our work, we perform a sensitivity experiment, and its result shows clearly an opposing response. Inline, the Arctic Dipole is likely to create Northerly winds in the Barents Sea, and therefore, as simulated, a westward transport South of Svalbard. This transport goes in the opposite direction as that of the BSO flow, if the later is defined as positive when entering the Barents Sea. The conclusions from Polyakov et al. (2023) also contradict the correlation between AD and BSO, from their very own dataset: based on the AD data from their Figure 2, and the BSO flow data from their Figure 3, one finds a clear negative correlation between the two time series, especially for the recent years. For the time period 2005-2021, the correlation between the two time series is -0.38, and for the time period 2011-2021 it reaches -0.53. These results are therefore in agreement with our findings (Figure 8).
On the other hand, our results are inline with R. B. Ingvaldsen et al. (2004), as adding a positive AD to the mean SLP actually exhibits an SLP pattern that looks similar to their Fig12b. However, according to our model experiments, the trend in AD (Figure 8) can not explain the BSO flow trend as the respective changes have an opposing effect on the BSO flow than the trend obtained when applying the full forcing (Figure 8). Note that a control experiment considered only AD-related winds north of 75°N. The result is very similar to using the full fields over the Northern Hemisphere, although the sensitivity of the BSO flow is weaker.
When applying the first leading mode, i.e. the AO pattern, the model response appears weaker compared with the response to the AD pattern. However, a weakening AO mode does well produce a significant increase in BSO flow as the wind patterns related with a strong positive AO, are associated with Easterlies (Figure 7a) in the BSO, and therefore with an outflow pattern. This finding seems consistent with the BSO-trend, but the effect is much too weak - especially since the AO only exhibits a very weak trend over the considered time period. The simulated increase of the BSO flow when using the full atmospheric forcing is more than 20%, whereas a positive AO vs a negative AO explains only 8% while the observed AO trend is much weaker than considering the difference between positive and negative AO phases. Therefore, we conclude that the BSO flux trend can not be explained either by the changes of the leading atmospheric modes over the Arctic.

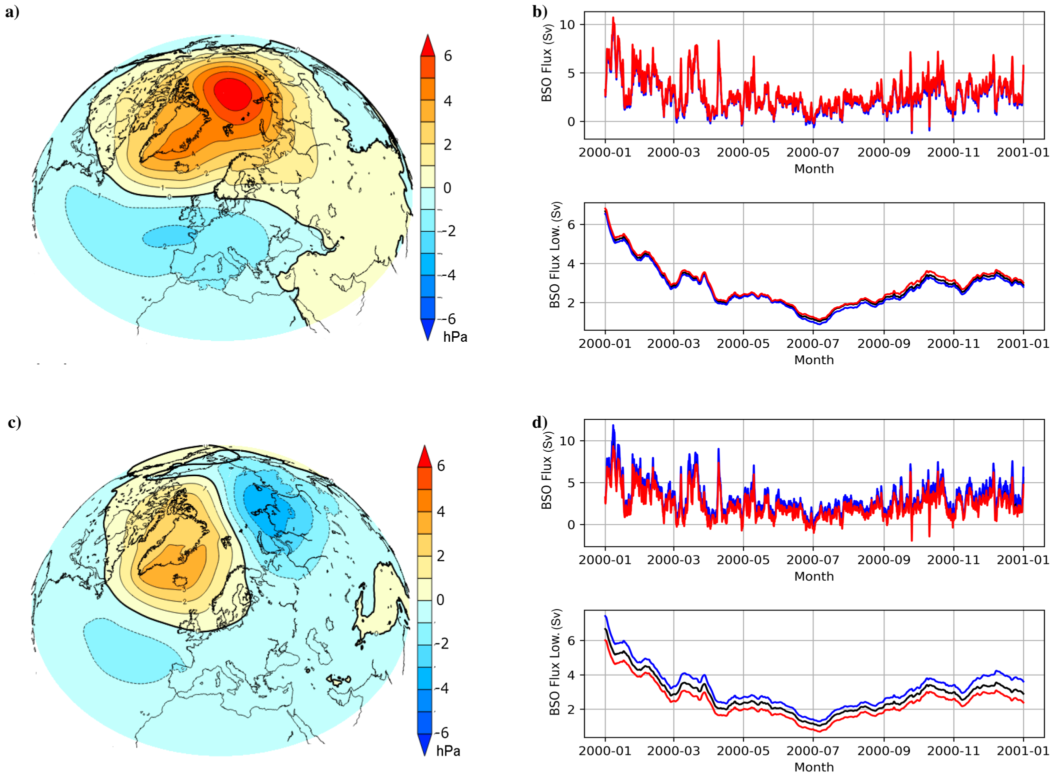

Figure 7. a) Arctic Oscillation SLP pattern (AO-), which corresponds to its first EOF b) BSO flow for year 2000, black is the reference simulation, blue is the simulation corresponding with the AO negative anomaly (AO- run hereafter), red is the simulation corresponding with the AO positive anomaly (AO+ run hereafter). The reference, AO-, AO+ mean BSO fluxes are 2.8 Sv, 2.92 Sv and 2.69 Sv respectively. c) Arctic Dipole, which corresponds to EOF2 of the SLP above 70N, mean value of the period 1979-2022. d) BSO flow for year 2000, black is the reference forcing, blue is the simulation corresponding with the AD negative anomaly (AD- run hereafter), red is the simulation corresponding with the AD positive anomaly (AD+ hereafter). The reference, AD-, AD+ mean BSO fluxes are 2.8 Sv, 3.22 Sv and 2.41 Sv respectively.

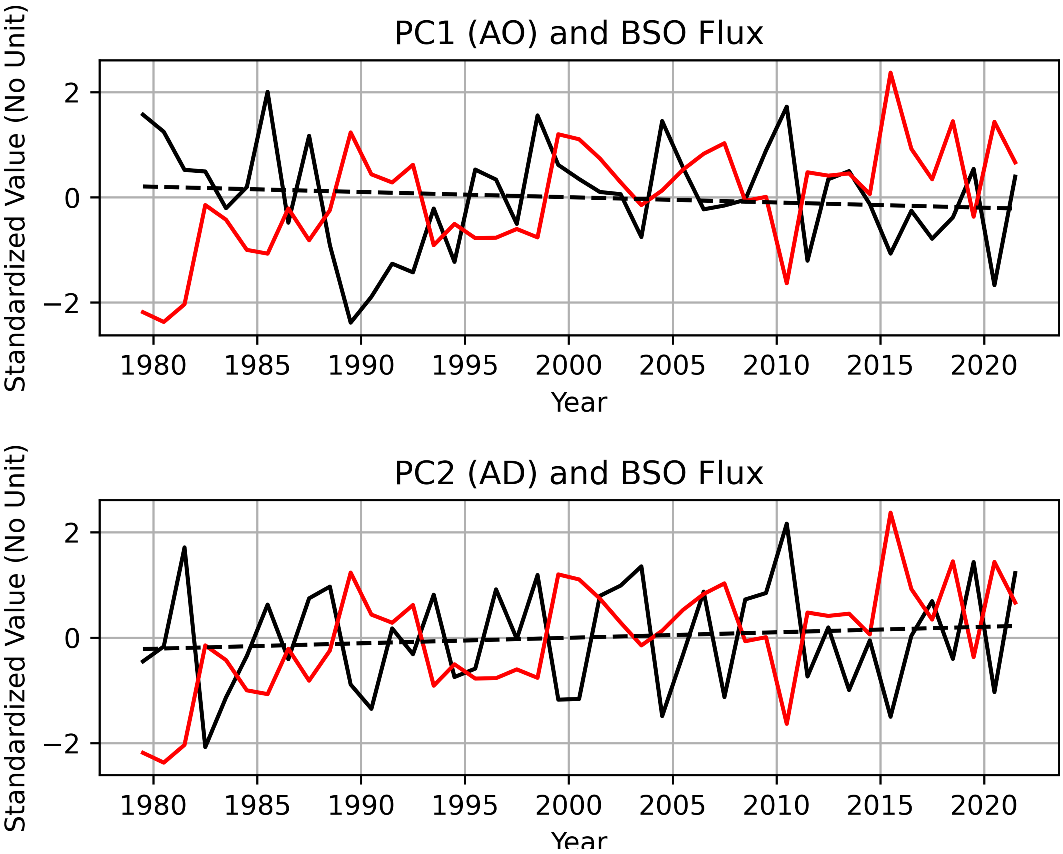

Figure 8. Principal components of the AO and the AD (Black plain line, dashed line for the linear trend) and the BSO flow (Red). Annual mean values for the period 1979-2021. The principal components and the BSO flow are standardized by subtracting their mean values, and dividing by their standard deviation. At a monthly timescale, the relation between the two Arctic leading modes and the BSO flow appears obvious. The correlation between the BSO flow and the AD is -0.75 whereas the correlation with the AO is only -0.24. At an annual timescale, the correlation between the BSO flow and the AD is -0.42, but that with the AO becomes -0.55. The trend in AD and AO, are 0.09 and -0.15 for the time period 1979-2021 respectively. Based on an EOF value of 500 Pa, this corresponds to a difference of 45 and 75 Pa, respectively.

5 Discussion and Conclusion

The results presented in Figure 2 show that there is a positive trend of flow at BSO, from the Nordic Seas towards the Barents Sea. At the scale of the Nordic Sea basins, this trend is compensated by other flow trends at other gates. Therefore, the causality link can not be established directly: the BSO flow trend could be very well driven from further South and pushed for example by a stronger flow at Faroe-Shetland strait, itself resulting from a stronger meridional transport. Through the utilization of a DL model, that takes for input wind time series resulting from a spatial average done over specific areas of the Nordic Seas, we can establish a link between the trend of the BSO flow and atmospheric wind forcing over the Nordic Seas area. We find that the BSO flow and its trend can be reconstructed only if the Deep Learning pipeline is fed by high frequency wind data (one to three hours sampling period) over a period of 3 weeks prior to the time of the reconstruction. This link proves that within the wind time series extracted from the Nordic Seas forcing, the source of the BSO flow trend is present. And we provide a reasoning that shows that the BSO flow trend comes most likely only from the wind forcing over this area, which excludes another causality. In addition, sensitivity tests based on the DL model confirm that the BSO flow is sensitive to the meridional wind and Sverdrup transport in the Nordic Seas basin, which means that a higher vorticity in the Nordic Seas increases the BSO flow. The limitation of our DL approach is that, per se, it does not provide an understanding of the underlying physical processes that drive the BSO flow trend. Rather, it is a mean to explore non-linear statistical links and as such it provided information on potential drivers and respective timescales.

In order to identify the physical processes behind the statistical links identified by the DL, we performed idealized experiments with the prognostic general ocean circulation model that explored the impact of wind changes that are related to known changes in the leading atmospheric modes over the North Atlantic and the Arctic. Our results indicate that changes in the NAO and EA-pattern (i.e. the two leading modes of sea level pressure anomalies over the North Atlantic) from 1979-1988 to 2013-2022 have a very weak impact on the simulated BSO flow as even the sign is not consistent with the simulated trend of the full simulation. The impact of NAO patterns in our simulation is difficult to compare with the results of Muilwijk et al. (2019), who used strong or weak NAO anomalies, whereas we used real NAO trends. But our findings confirm the work of Smedsrud et al. (2013); Heukamp et al. (2023); Polyakov et al. (2023), that show a weak NAO influence on the BSO flow. For the Arctic Ocean, we focused on changes over time and did not refer to pattern changes. This approach was triggered by foregoing studies that highlighted the potential importance of the AD and its changes over time. We found that both, pronounced AO and AD positive phases, can lower the BSO flow. As suggested earlier by Polyakov et al. (2023), the AD had a relatively pronounced impact on the BSO flow, but the known trend in the AD goes into the wrong direction. Moreover, the relation between AD and BSO flow is anti-correlated both in the present work and in Polyakov et al. (2023). We therefore conclude that the trend in AD can not explain the trend in BSO flow.
The trend in the AO, in contrast, would go into the right direction and the ongoing weakening trend of AO can lead to a higher BSO flow. The latter can be explained by the fact that a weaker AO would lead to weaker Easterly winds in the Northern part of BSO. A weaker AO would lead to a weaker outflow, consistent with our model results showing that the BSO positive trend is mostly due to a smaller outflow from the Barents Sea towards the Nordic Seas (Figure 3). This implies that the change in the total flow is more related to the decreasing outflow than the change in inflow. That said, the respective observed trend in the AO is too weak to have a strong impact. For illustration, considering a shift from an AO plus to AO negative phase would refer to an approx 8% change in the BSO flow while the observed AO trend is rather minor. The increase of the simulated BSO flow represented by Nemo-NAA10km with full atmospheric forcing is more than 20%.

We conclude that it is likely that the atmospheric patterns that lead to the simulated trend in BSO flow when applying the full atmospheric forcing, are relatively complex and do not project directly on the leading modes of atmospheric variability over the North Atlantic and the Arctic. Further experiments, out of scope with the present manuscript, show that the BSO flow trend can not be explained by a linear trend of atmospheric variability. Using an atmospheric forcing from which the linear trend of wind velocity and atmospheric pressure has been removed, produces a BSO flow trend which value is 97% of that computed with the normal atmospheric forcing, showing that the BSO flow trend is driven by a non-linear process.
Our speculations are inline with the findings of Muilwijk et al. (2019), as we relate anomalous BSO flows to a very specific atmospheric pattern identified by using climate response functions, and Heukamp et al. (2023), who refer to the importance of the local cyclonic activity. Also, (potentially complex) interactions in the leading atmospheric modes as well as the impact of sea ice decline are not captured in the presented study (see for example Koenigk et al. (2009) for potential feedback mechanisms in coupled simulations). Note, however, that the DL approach could reconstruct the simulated trend in the BSO flow to a large degree when considering ice free areas only.
In summary, we failed to identify the underlying pattern "hidden" in the wind data that can explain the BSO flow trend. Utilizing a DL model, however, ensures that what leads to the simulated BSO flow trend is related to some signal in the wind data time series provided to the DL model. We can also confirm that wind over the Nordic Seas can explain this trend, since it is the only geographical source of the time series. It also gives us a hint to search more towards high frequency processes. Therefore, some additional research is needed.

6 Open Research

The data used in this article is available online in the following repository
https://ns5001k.web.sigma2.no/2024JC021663/
Sigma2 is the Norwegian Infrastructure for High-Performance Computing and Data Storage in Norway.

Acknowledgments

The research of V. Jahanmard was supported by the Estonian Research Council grants PRG1785 "Development of continuous DYNAmic vertical REFerence for maritime and offshore engineering by applying machine learning strategies/DYNAREF/" and N.Delpeche-Ellmann by PRG1129. This work was supported by the Bjerknes Centre for Climate Research through the project SKD-DYNASOR. This work was also supported by Copernicus ARC MFC. The ocean modelling work of Robinson Hordoir was supported by the Bjerknes Centre Model Development Activity, and by the Fram Centre program for Sustainable Development of the Arctic Ocean (SUDARCO) Cristin-ID: 2551323.
Ulrike Löptien and Heiner Dietze acknowledge funding by the DFG project "Projecting critical coastal oxygen deficits by the example of the Eckernfrde Bight (grant number 491008639).
The computations used in this research work were performed on resources provided by Sigma2 - the National Infrastructure for High-Performance Computing and Data Storage in Norway.

Appendix A Deep Learning Model

As outlined in section 3, to address the prediction of temporal BSO flow variation, we developed a multivariate causal convolutional neural network (Oord et al., 2016; Bai et al., 2018). We choose a rather complex DL architecture since we expected large non-

linearities and additionally wanted to cover time dependencies. Other common and simpler time series neural network architectures that cover time dependencies, such as Long short-term memory network (LSTM) and Multilayer Perceptrons (MLP), were tested for our purpose (Granata & Di Nunno, 2023; Yi et al., 2024; Hochreiter & Schmidhuber, 1997; K. Chen et al., 2021; Che et al., 2018). However, in our benchmarking, the causal convolutional network is selected because of its smaller generalization errors (shown in Figure A2). The selected model architecture facilitates efficient feature learning from a sequence of input variables, unlike the LSTM models that require more measures to be taken into account to reduce overfitting (Kinoyama et al., 2021).
Please note that, in contrast to basic machine learning research the focus here is not on developing deep learning architectures (such as outcompeting other approaches) but, rather, to apply a tested framework to obtain scientific hypotheses which are then fed into further analysis and a first-principle model for testing. The causal term in convolutional layers refers to using past data to reconstruct each moment, without any information leakage from the future to the past. However, due to the inherent directed acyclic graph (DAG) structure of the deep neural networks, the DL model can propose a causal inference between input variables and the output (Cui & Athey, 2022; Wang et al., 2022; Berrevoets et al., 2023). The physical causality between the wind indexes and the BSO flow arises based on expert knowledge of physics that indicates the relation between them is cause and effect. It should be noted that there are no effect variables of the BSO flow inside the input variables. On the other hand, by reducing the generalization error, it can be deduced that the model suggests a causal inference for the BSO flow, which can enable further investigation into the variability of BSO flow under the influence of wind indexes.

The model comprises a series of causal convolution layers for extracting features from lags of inputs within a period of historical data (receptive field of RF). This is followed by a stack of dense layers designed to perform regression on these features to predict the hourly BSO flow. During the training process, the learnable parameters, including weights and biases, of layers, such as convolution and dense layers, are tuned to predict the BSO flow using features extracted from the lags of wind data within an RF.

Increasing RF size allows for the inclusion of information from a wider range of past wind data and captures long-term dependencies. Figure A1 illustrates the architecture of the DL model, comprising k residual blocks of causal convolutions followed by p blocks of fully connected layers. Therefore, the length of RF is determined as follows:

$$RF = (fs - 1)(2^k - 1) + 1 \tag{A1}$$

where fs is the filter size of the convolutional layers and is set to 2. Adam optimizer is used for gradient descent learning. Hyperparameters were tuned through grid search, which as a result, our DL model architecture includes 128 filters in each convolutional layer, 64 nodes in the fully connected layers, a dropout probability of 0.25, and two blocks of fully connected layers (see Figure A1). The number of residual blocks of causal convolutions k (which reflects the length of the RF according to Equation A4) was selected based on the model's ability to reconstruct the BSO long-term trend. Hence, the model was optimized for each k individually (shown in Figure 5). For this purpose, trend ratio TR is defined as the ratio of the predicted trend to the actual trend. As a result, the number of residual blocks was set to 9, which indicates that 3 weeks of past data are used to predict the BSO flow. The dataset was divided into training (80%, from the first of 1975 to 2011), validation (15%, from 2012 to 2019), and testing (5%, the last two years) sets. For stable training, input variables are normalized to a range of 0 to 1. Target values are kept in their original scale, consequently, a learning rate of 4 was determined from the grid search. The training process was monitored using the validation set to avoid overtraining with a patience value of 10. The model is trained in epochs of 136.

Therefore, the input variables of size c are sequentially fed into k residual blocks, each consisting of a dilated causal convolution, batch normalization, and Rectified Lin-

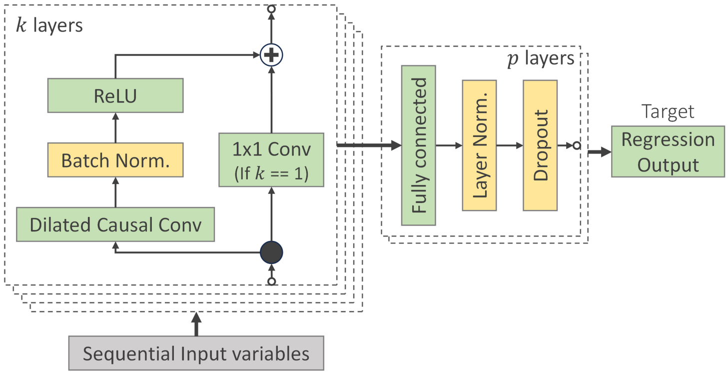

Figure A1. Diagram representing the DL model architecture with k residual blocks of causal convolutions and p blocks of fully connected layers.

ear Unit (ReLU) activation layer. The residual block is a non-linear module where the output is formed by adding the input, which is able to address the gradient vanishing problem and improve learning efficiency in deep learning architectures (He et al., 2016). Incorporating dilated causal convolution layers into the model facilitates an increase in the receptive field size RF without significantly raising the number of learnable parameters or the computational cost (Oord et al., 2016). The dilation factor for each block is set to $d = 2^{(k-1)}$. Therefore, the output of the k-th residual block ($k > 1$) for the i-th filter ($i = 1, 2, ..., nf$) at time step t is:

$$\begin{gathered}\hat{z}_k[i,t] = \gamma_k[i] \cdot \frac{\sum_{q=1}^{fs}\sum_{j=1}^{fs} w_k[q,j,i] \cdot z_{k-1}[j, t-d(q-1)] + b_k[i] - \mu_k[i]}{\sqrt{\sigma_k^2[i] + \epsilon}} + \beta_k[i] \\ z_k[i,t] = \mathrm{ReLU}\left(\hat{z}_k[i,t]\right) + z_{k-1}[i,t]\end{gathered} \tag{A2}$$

where z_k and z_{k-1} are the outputs and inputs of the module. The indices q and j in the summations correspond to the filter size and input feature size, respectively. The first residual block includes a skip causal convolution layer with a filter size of one to maintain dimensional consistency. Therefore, for $k = 1$:

$$\begin{gathered}\hat{z}_1[i,t] = \gamma_1[i] \cdot \frac{\sum_{q=1}^{fs}\sum_{j=1}^{c} w_1[q,j,i] \cdot x[j, t-d(q-1)] + b_1[i] - \mu_1[i]}{\sqrt{\sigma_1^2[i] + \epsilon}} + \beta_1[i] \\ z_1[i,t] = \mathrm{ReLU}\left(\hat{z}_1[i,t]\right) + \sum_{j=1}^{c} w_0[1,j,i] \cdot x[j,t] + b_0[i]\end{gathered} \tag{A3}$$

where weights w_k and bias b_k are trainable parameters of the convolution layers with the filter size fs and the number of filters nf. The convolution outputs are normalized using batch normalization with learnable scale parameters γ and shift parameters β. The mean and standard deviation of the convolution layer outputs are denoted as μ and σ, respectively. ReLU activation function is applied after the batch normalization layer to introduce non-linearity, enabling the model to capture intricate data features and patterns (Sharma et al., 2017). The ReLU function outputs zero for negative input values and retains positive ones unchanged.

The fully connected layers integrate the features extracted by the convolutional blocks and transform them into the final prediction. Let $x \in \mathbb{R}^m$ be the input to the fully connected layer and $y \in \mathbb{R}^n$ be the output of the layer, therefore:

$$y(t) = \mathbf{w}x(t) + \mathbf{b} \tag{A4}$$

Table A1. Summary of the DL model. Output shape indicates the dimension of layer output in batches (B), time steps (T), and channels (C).

	Layer Name	Layer Type	Output Shape	Learnable Parameters
	Sequential_Inputs	Input	1(B) × 1(T) x 27(C)	-
k = 1	Dilated_Causal_Conv_01	Conv1D	1(B) $\times 1(T) \times 128(C)$	2 $\times 27 \times 128(w) + 128(b)$
	BatchNorm_01	Batch Normalization	1(B) $\times 1(T) \times 128(C)$	128 (Offset) + 128 (Scale)
	ReLU_01	ReLU		-
	Skip_Conv	Conv1D	1(B) $\times 1(T) \times 128(C)$	2 $\times 27 \times 128(w) + 128(b)$
	Add_01	Addition	1(B) $\times 1(T) \times 128(C)$	-
k = 2,...,9	Dilated_Causal_Conv_(k)	Conv1D	1(B) $\times 1(T) \times 128(C)$	2 $\times 128 \times 128(w) + 128(b)$
	BatchNorm_(k)	Batch Normalization	1(B) $\times 1(T) \times 128(C)$	128 (Offset) + 128 (Scale)
	ReLU_(k)	ReLU		
	Add_(k)	Addition	1(B) $\times 1(T) \times 128(C)$	-
p = 1	Dense_01	Fully Connected	1(B) $\times 1(T) \times 64(C)$	64 $\times 128(w) + 64(b)$
	LayerNorm_01	Layer Normalization	1(B) $\times 1(T) \times 64(C)$	64 (Offset) + 64 (Scale)
	Dropout_01	Dropout	1(B) $\times 1(T) \times 64(C)$	-
p = 2	Dense_01	Fully Connected	1(B) $\times 1(T) \times 64(C)$	64 $\times 64(w) + 64(b)$
	LayerNorm_02	Layer Normalization	1(B) $\times 1(T) \times 64(C)$	64 (Offset) + 64 (Scale)
	Dropout_02	Dropout	1(B) $\times 1(T) \times 64(C)$	-
	Output	Fully Connected	1(B) $\times 1(T) \times 1(C)$	1 $\times 64(w) + 64(b)$

Number of layers: 46

Total learnable parameters: 288.8k

Optimizer: Adam

where $\mathbf{w} \in \mathbb{R}^{n \times m}$ and $\mathbf{b} \in \mathbb{R}^n$ are learnable weight and bias of the fully connected layer, respectively. We used layer normalization after the fully connected layers to stabilize training and a dropout layer to improve model generalization. Table A1 presents a list of the layers used in the model in detail. The loss function is the half-mean-squared-error of the predicted flow for each time step:

$$Loss = \frac{1}{2N} \sum_{j}^{N} (T_j - y_j)^2 \tag{A5}$$

where N is the length of the sequence in each sample. In the training process, the time series was segmented into samples of two years, with a one-month overlap between consecutive samples. This interval is sufficiently long to have a smooth and stable training on samples, yet not so extended as to reflect the BSO long-term trend. We used a mini-batch size of 6, which results in four iterations per epoch. The evolution of the loss function is demonstrated in Figure A2b. The target values are unscaled, with an order of magnitude of 1e6 in this version of the DL model. The learning rate and L2 regularization were optimized via grid search. No overshooting in training loss was observed during the initial iterations, suggesting the learning rate is appropriately set. The gradual decrease in loss throughout the iterations further indicates stable convergence.

Figure A2a shows the predicted flow for the training set in blue and the (validation and) test set in red compared with the target BSO flow obtained from the Nemo-

NAA10km model. Performance of the DL model is presented in Figure A2c and d through a scatter plot of target vs. predicted BSO flow. As a result, the model predicts the BSO flow with an RMSE of 5.03e5 Sv and 6.52e5 Sv for the training and test sets, respectively. The R^2 values of 0.91 for the training set and 0.81 for the test set indicate that the model was generalized appropriately. However, the model has not yet excelled in capturing extreme events, and further considerations are required to improve the DL model for both extreme low and high events. We repeated the training of the DL model multiple times and observed consistent performance in both the training and test sets, indicating that the model is stable and has been sufficiently trained. Henceforth, the entire dataset is utilized to train the DL model to accurately capture the BSO long-term trend for use in subsequent experiments.

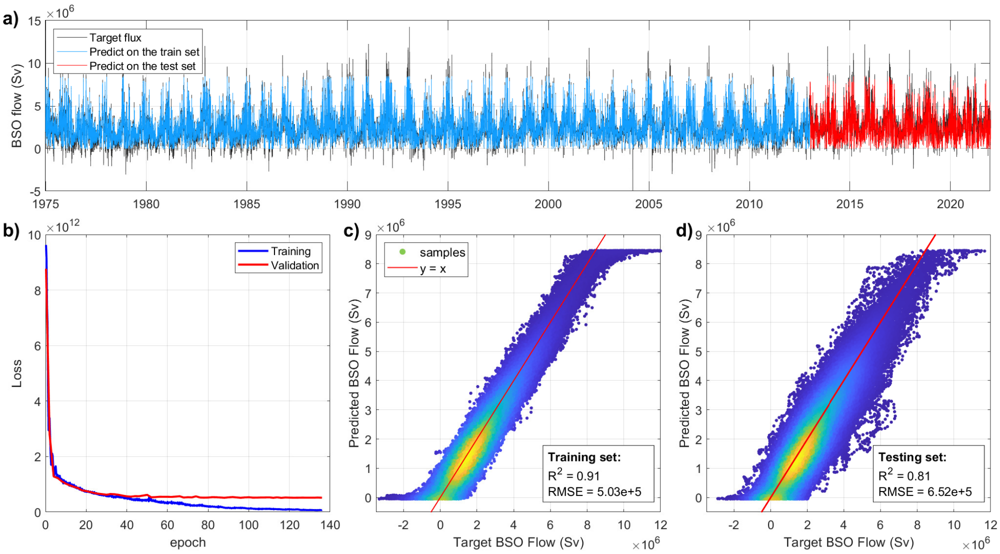

Figure A2. DL Model Training Results. a) Comparison of target and predicted BSO flow on the training and test sets for an RF of 3 weeks. b) Training and validation loss as a function of training epochs. Panels (c) and (d) demonstrate density scatter plots showing target vs. predicted flow for training and testing sets, respectively.

A1 Explaining DL Model Predictions

The field of Explaining AI is broad, as it simultaneously needs to address different types of machine learning models and a wide range of interpretability requirements (Letzgus et al., 2022). In this study, we conducted a series of experiments, including retraining the model by disturbing input features or using combinations of input features, and input perturbation analysis to identify the sensitivity of the model to input variables.

Figure A3a shows the BSO flow prediction using the DL model with all 27 wind indexes. The model successfully reconstructs the flow, achieving an R^2 value of 0.97 and a TR of 0.92. However, the predicted flow contains a bias (Figure A3c), which can be attributed to the model's capacity to accurately predict extreme events. In addition, Figure A3b presents the annual mean of both actual and predicted flows. To demonstrate the outcomes of the model, we also present results obtained through training with different subsets of wind indexes. By excluding wind indexes from "500m isobath" and "All Nordic Sea" boxes, the DL model reconstructs the flux with an R^2 of 0.96 and a TR of 0.93, which is almost the same result as using all wind indexes. Training the DL model exclusively with wind indexes from the "500m isobath" and "BSO boxes" yielded an R^2 of 0.94 and a TR of 0.80. The long-term trend of the latest model can be improved by including wind indexes of Fram Strait into the input variables, which results in R^2 of 0.95 and TR of 0.91.

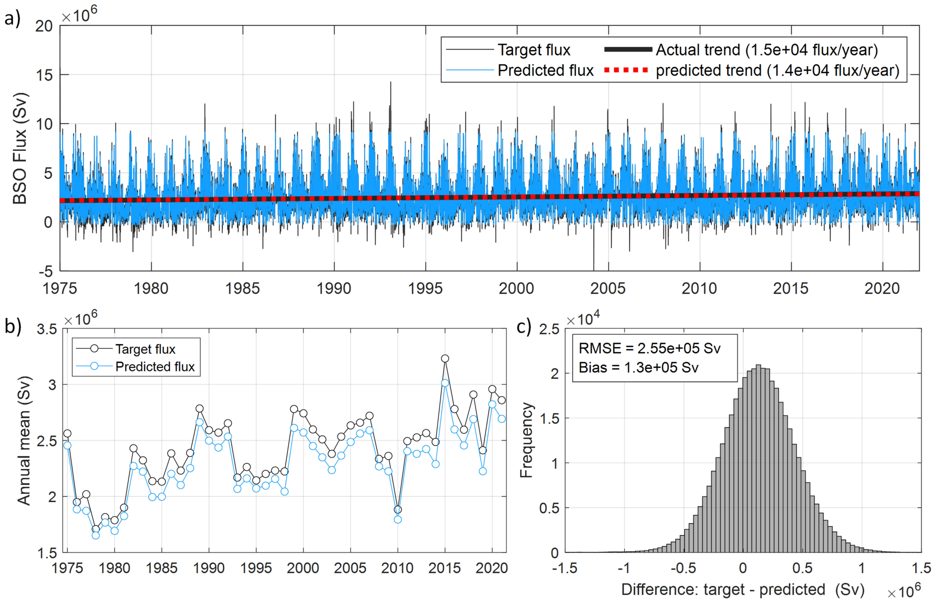

Figure A3. a) Reconstructed BSO flow using all wind components and RF of 3 weeks. The black line represents the long-term trend of the actual BSO flow, while the red dashed line corresponds to the predicted BSO flow. The DL model successfully reconstructed the long-term trend with a TR value of 0.92. b) annual mean flux of actual and predicted time series. c) histogram of differences between actual and predicted BSO flux.

Training the DL model only with wind indexes from BSO gates resulted in an R^2 of 0.91 and a TR of 0.78. This shows that the model reconstructs a substantial portion of the long-term trend with solely wind data from BSO gates. However, training the DL model with all available indexes except those from BSO gates can still result in an R^2 of 0.96 and a TR of 0.90, which demonstrates that information for capturing the long-term trend can also be obtained from other locations than BSO gates. Therefore, further investigation into features using feature selection methods may not provide additional insights into the drivers of the BSO flow trend, as the RF of 3 weeks is sufficient to observe events across all locations and the model is able to establish relationships with the remaining features. Hence, using all 27 features is more suitable for training a more stable model. In addition, We want to emphasize at this point that providing more features adds information for the DL model to provide a better representation of the BSO flow, but that it is at this stage impossible to establish a connection with the underlying physical processes that drive the BSO flow trend.

Incorporating wind indexes from different locations enables us to implicitly introduce spatial variability in wind patterns into the DL model, thereby enhancing the model's robustness. To assess the robustness of the DL model in the presence of noisy data, we retrained the DL model by adding random Gaussian noise to all inputs with a noise level of 10 percent of each input's standard deviation. The results showed almost consistent performance in reconstructing the flow. This observation suggests that the model can find the solution within noisy data by establishing relations between the lags and locations of the wind indexes. In another experiment, we disrupted the frequency dependencies among input variables by performing a fast Fourier transform (FFT) on the wind indexes and then combining the components with random phases. Training the model with this artificially modified wind data demonstrated that the model was unable to reconstruct the flow without the true frequency dependencies among the input variables.

The causal relationship between wind patterns and the BSO trend can be investigated by perturbing the input wind data and observing the output of the trained models. Due to our interest in the long-term trend of the BSO flow, a trend perturbation was applied to input variables by scaling the long-term trend of each variable by α. The perturbed input variables are determined by adding a trend of $\alpha.t/(46years)$, where t is time with the reference epoch of 1975.0 and the factor α ranges from -0.05 to 0.05 in increments of 0.01.

Figure A4 presents the results of trend perturbation, demonstrating how changes in the long-term trend of each input variable (for different regions in the study area) impact the TR of the predicted BSO long-term trend. This figure shows strong positive correlations in the DL model, indicating that increasing long-term trends of the BSO gate wind stress and northward wind stress in "500m isobath" correspond to increased long-term trends in BSO flow predictions. Furthermore, notable inverse correlations are evident with the eastward wind stress in "All Nordic Sea" and the northward wind stress in Fram Strait and Iceland-Faroe gate. Generally, the perturbation analysis indicates that an increase in the long-term trend of northward wind stresses in the eastern and southeastern regions of the study area can result in an upsurge in the BSO trend. Conversely, an increasing trend in the Fram Strait wind indexes can lead to a reduction in the BSO trend. It is important to note that the introduced trends in the input wind indexes are of a small magnitude, so that applying an α of 0.01 is equivalent to 1% of the wind range.

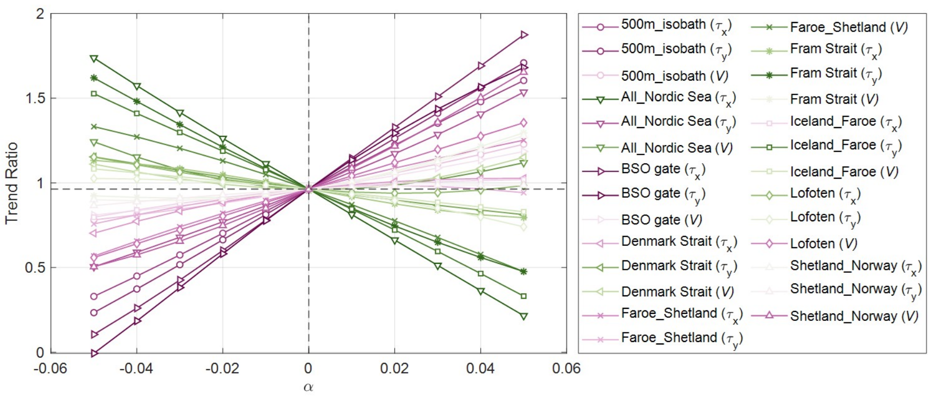

Figure A4. Trend perturbation test on the trained DL model with actual wind data.

References

Ådlandsvik, B., & Loeng, H. (1991). A study of the climatic system in the barents sea. *Polar Research*, *10*, 4549. Retrieved from `https://doi.org/10.3402/polar.v10i1.6726` doi: 10.3402/polar.v10i1.6726

Årthun, M., Ingvaldsen, R., Smedsrud, L., & Schrum, C. (2011). Dense water formation and circulation in the Barents Sea. *Deep Sea Research Part I: Oceanographic Research Papers*, *58*(8), 801817. Retrieved from http://www.sciencedirect.com/science/article/pii/S096706371100104X doi: 10.1016/j.dsr.2011.06.001

Bai, S., Kolter, J., & Koltun, V. (2018). An empirical evaluation of generic convolutional and recurrent networks for sequence modeling. *arXiv preprint arXiv:1803.01271*. doi: https://arxiv.org/abs/1803.01271

Barnston, A. G., & Livezey, R. E. (1987). Classification, seasonality and persistence of low-frequency atmospheric circulation patterns. *Monthly Weather Review*, *115*(6), 1083 - 1126. Retrieved from https://journals.ametsoc.org/view/journals/mwre/115/6/1520-0493_1987_115_1083_csapol_2_0_co_2.xml doi: 10.1175/1520-0493(1987)115⟨1083:CSAPOL⟩2.0.CO;2

Bengtsson, L., Semenov, V. A., & Johannessen, O. M. (2004). The early twentieth-century warming in the arctica possible mechanism. *Journal of Climate*, *17*(20), 40454057. Retrieved from https://doi.org/10.1175/1520-0442(2004)017<4045:TETWIT>2.0.CO;2 doi: 10.1175/1520-0442(2004)017⟨4045:TETWIT⟩2.0.CO;2

Berrevoets, J., Kacprzyk, K., Qian, Z., & van der Schaar, M. (2023). Causal deep learning. Retrieved from http://arxiv.org/pdf/2303.02186

Blindheim, J. (1989). Cascading of barents sea bottom water into the norwegian sea. *Rapports et Proce's-verbaux des Re unions du Conseil International par lExploration de la Mer*, *188*, 49-58.

Brajard, J., Carrassi, A., Bocquet, M., & Bertino, L. (2020). Combining data assimilation and machine learning to emulate a dynamical model from sparse and noisy observations: A case study with the lorenz 96 model. *Journal of Computational Science*, *44*, 101171. Retrieved from https://www.sciencedirect.com/science/article/pii/S1877750320304725 doi: https://doi.org/10.1016/j.jocs.2020.101171

Chafik, L., Nilsson, J., Skagseth, ., & Lundberg, P. (2015). On the flow of atlantic water and temperature anomalies in the nordic seas toward the arctic ocean. *Journal of Geophysical Research: Oceans*, *120*(12), 7897-7918. Retrieved from https://agupubs.onlinelibrary.wiley.com/doi/abs/10.1002/2015JC011012 doi: https://doi.org/10.1002/2015JC011012

Che, Z., Purushotham, S., Cho, K., Sontag, D., & Liu, Y. (2018, April). Recurrent neural networks for multivariate time series with missing values. *Scientific Reports*, *8*(1). Retrieved from http://dx.doi.org/10.1038/s41598-018-24271-9 doi: 10.1038/s41598-018-24271-9

Chen, J., Song, L., Wainwright, M., & Jordan, M. (2018). Learning to explain: An information-theoretic perspective on model interpretation. In *International conference on machine learning* (pp. 883–892).

Chen, K., Kuang, C., Wang, L., Chen, K., Han, X., & Fan, J. (2021). Storm surge prediction based on long short-term memory neural network in the east china sea. *Applied Sciences*, *12*(1), 181.

Cui, P., & Athey, S. (2022, February). Stable learning establishes some common ground between causal inference and machine learning. *Nature Machine Intelligence*, *4*(2), 110115. Retrieved from http://dx.doi.org/10.1038/s42256-022-00445-z doi: 10.1038/s42256-022-00445-z

Cuny, J., Rhines, P. B., & Ron Kwok. (2005). Davis strait volume, freshwater and heat fluxes. *Deep Sea Research Part I: Oceanographic Research Papers*, *52*(3), 519542. Retrieved from https://www.sciencedirect.com/science/article/pii/S0967063704002134 doi: 10.1016/j.dsr.2004.10.006

de Boer, A. M., Gavilan Pascual-Ahuir, E., Stevens, D. P., Chafik, L., Hutchinson, D. K., Zhang, Q., . . . Willmott, A. J. (2018). Interconnectivity between volume transports through arctic straits. *Journal of Geophysical Research: Oceans*, *123*(12), 8714-8729. Retrieved from https://agupubs.onlinelibrary.wiley.com/doi/abs/10.1029/2018JC014320 doi: https://doi.org/10.1029/2018JC014320

Deser, C. (2000). On the teleconnectivity of the arctic oscillation. *Geophysical Research Letters*, *27*(6), 779-782. Retrieved from `https://agupubs.onlinelibrary.wiley.com/doi/abs/10.1029/1999GL010945` doi: https://doi.org/10.1029/1999GL010945

Diebold, F. (2007). Elements of forescasting. *Thomson South-Western*, 230231.

Dietze, H., & Löptien, U. (2021). Retracing hypoxia in eckernförde bight (baltic sea). *Biogeosciences*, *18*, 4243-4264. doi: 10.5194/bg-18-4243-2021

Dmitrenko, I. A., Rudels, B., Kirillov, S. A., Aksenov, Y. O., Ivanov, V. V., Schauer, U., … Barber, D. (2015). Atlantic water flow into the arctic ocean through the st. anna trough in the northern kara sea. *Journal of Geophysical Research*, *120*(7), 5158-5178. Retrieved from `https://doi.org/10.1002/2015JC010804` doi: 10.1002/2015JC010804

Fossheim, M., Primicerio, R., Johannesen, E., Ingvaldsen, R. B., Aschan, M. M., & Dolgov, A. V. (2015, Jul 01). Recent warming leads to a rapid borealization of fish communities in the Arctic. *Nature Climate Change*, *5*(7), 673-677. Retrieved from `https://doi.org/10.1038/nclimate2647` doi: 10.1038/nclimate2647

Gill, A. (1982). *Atmosphere-ocean dynamics*. Academic Press.

Gogina, M., & Zettler, M. L. (1999). Investigating causal relations by econometric models and cross-spectral methods. *Econometrica*, *37*(3), 424-438.

Granata, F., & Di Nunno, F. (2023). Neuroforecasting of daily streamflows in the uk for short-and medium-term horizons: A novel insight. *Journal of Hydrology*, *624*, 129888.

He, K., Zhang, X., Ren, S., & Sun, J. (2016). Deep residual learning for image recognition. In *Proceedings of the ieee conference on computer vision and pattern recognition* (pp. 770–778).

Heo, E.-S., Sung, M.-K., An, S.-I., & Yang, Y.-M. (2021). Decadal phase shift of summertime arctic dipole pattern and its nonlinear effect on sea ice extent. *International Journal of Climatology*, *41*(9), 4732-4742. Retrieved from `https://rmets.onlinelibrary.wiley.com/doi/abs/10.1002/joc.7097` doi: https://doi.org/10.1002/joc.7097

Herbaut, C., Houssais, M.-N., Close, S., & Blaizot, A.-C. (2017). On the spatial coherence of the atlantic water inflow across the nordic seas. *Journal of Geophysical Research: Oceans*, *122*(5), 4346-4363. Retrieved from `https://agupubs.onlinelibrary.wiley.com/doi/abs/10.1002/2016JC012566` doi: https://doi.org/10.1002/2016JC012566

Heukamp, F. O., Aue, L., Wang, Q., Ionita, M., Kanzow, T., Wekerle, C., & Rinke, A. (2023, Sep 21). Cyclones modulate the control of the north atlantic oscillation on transports into the barents sea. *Communications Earth & Environment*, *4*(1), 324. Retrieved from `https://doi.org/10.1038/s43247-023-00985-1` doi: 10.1038/s43247-023-00985-1

Hilmer, M., & Jung, T. (2000). Evidence for a recent change in the link between the north atlantic oscillation and arctic sea ice export. *Geophysical Research Letters*, *27*(7), 989-992. Retrieved from `https://agupubs.onlinelibrary.wiley.com/doi/abs/10.1029/1999GL010944` doi: https://doi.org/10.1029/1999GL010944

Hochreiter, S., & Schmidhuber, J. (1997). 1997. long short-term memory. *Neural computation*, *9*(8), 1735-1780. doi: 10.1162/neco.1997.9.8.1735

Hordoir, R., Skagseth, ., Ingvaldsen, R. B., Sand, A. B., Löptien, U., Dietze, H., … Lind, S. (2022). Changes in Arctic stratification and mixed layer depth cycle: A modeling analysis. *Journal of Geophysical Research: Oceans*, *127*(1). doi: https://doi.org/10.1029/2021JC017270

Hurrell, J. W. (1995). Decadal trends in the north atlantic oscillation: Regional temperatures and precipitation. *Science*, *269*(5224), 676-679. Retrieved from `https://www.science.org/doi/abs/10.1126/science.269.5224.676` doi:

10.1126/science.269.5224.676

Ingvaldsen, R. (2005). Width of the north cape current and location of the polar front in the western barents s. *Geophysical Research Letters*, *32*(16). Retrieved from https://doi.org/10.1029/2005GL023440 doi: 10.1029/2005GL023440

Ingvaldsen, R., Loeng, H., & Asplin, L. (2002). Variability in the atlantic inflow to the barents sea based on a one-year time series from moored current meters. *Continental Shelf Research*, *22*, 505-519.

Ingvaldsen, R. B., Asplin, L., & Loeng, H. (2004). Velocity field of the western entrance to the barents sea. *Journal of Geophysical Research: Oceans*, *109*(C3). Retrieved from https://agupubs.onlinelibrary.wiley.com/doi/abs/10.1029/2003JC001811 doi: https://doi.org/10.1029/2003JC001811

Jahanmard, V., Hordoir, R., Delpeche-Ellmann, N., & Ellmann, A. (2023). Quantification of hydrodynamic model sea level bias utilizing deep learning and synergistic integration of data sources. *Ocean Modelling*, *186*, 102286. Retrieved from https://www.sciencedirect.com/science/article/pii/S1463500323001269 doi: https://doi.org/10.1016/j.ocemod.2023.102286

Jung, T., Hilmer, M., Ruprecht, E., Kleppek, S., Gulev, S. K., & Zolina, O. (2003). Characteristics of the recent eastward shift of interannual nao variability. *Journal of Climate*, *16*(20), 3371 - 3382. Retrieved from https://journals.ametsoc.org/view/journals/clim/16/20/1520-0442_2003_016_3371_cotres_2.0.co_2.xml doi: 10.1175/1520-0442(2003)016⟨3371:COTRES⟩2.0.CO;2

Kinoyama, R., Perez, E. A. M., & Iba, H. (2021). Preventing overfitting of lstms using ant colony optimization. In *2021 10th international congress on advanced applied informatics (iiai-aai)* (pp. 343–350).

Koenigk, T., Mikolajewicz, U., Jungclaus, J. H., & Kroll, A. (2009, Jun 01). Sea ice in the barents sea: seasonal to interannual variability and climate feedbacks in a global coupled model. *Climate Dynamics*, *32*(7), 1119-1138. Retrieved from https://doi.org/10.1007/s00382-008-0450-2 doi: 10.1007/s00382-008-0450-2

Large, W. G., & Yeager, S. (2004). *Diurnal to decadal global forcing for ocean and sea-ice models : the data sets and flux climatologies* (Tech. Rep.). NCAR Technical Note, NCAR/TN-460+STR, CGD Division of the National Center for Atmospheric Research.

Letzgus, S., Wagner, P., Lederer, J., Samek, W., Müller, K.-R., & Montavon, G. (2022). Toward explainable artificial intelligence for regression models: A methodological perspective. *IEEE Signal Processing Magazine*, *39*(4), 40–58.

Lien, V. S., Schlichtholz, P., Skagseth, Ø., & Vikebø, F. B. (2017). Wind-driven atlantic water flow as a direct mode for reduced barents sea ice cover. *Journal of Climate*, *30*(2), 803-812. Retrieved from https://doi.org/10.1175/JCLI-D-16-0025.1 doi: 10.1175/JCLI-D-16-0025.1

Lien, V. S., Vikebø, F. B., & Skagseth, Ø. (2013). One mechanism contributing to co-variability of the atlantic inflow branches to the arctic. *Nature Communications*, *4*(1488). Retrieved from https://doi.org/10.1038/ncomms2505 doi: 10.1038/ncomms2505

Lind, S., Ingvaldsen, R., & Furevik, T. (2018). Arctic warming hotspot in the Northern Barents Sea linked to declining sea-ice import. *Nature Climate Change*, *8*(7), 634639. doi: https://doi.org/10.1038/s41558-018-0205-y

Mellado-Cano, J., Barriopedro, D., Garca-Herrera, R., Trigo, R. M., & Hernndez, A. (2019). Examining the north atlantic oscillation, east atlantic pattern, and jet variability since 1685. *Journal of Climate*, *32*(19), 6285 - 6298. Retrieved from https://journals.ametsoc.org/view/journals/clim/32/19/jcli-d-19-0135.1.xml doi: https://doi.org/10.1175/JCLI-D-19-0135.1

Midttun, L. (1985). Formation of dense bottom water in the barents sea. *Deep-Sea*

Research Part I, *32*, 1233-1241. Retrieved from https://doi.org/10.1016/0198-0149(85)90006-8 doi: 10.1016/0198-0149(85)90006-8

Mikhailova, N., & Yurovsky, A. V. (2016). The east atlantic oscillation: Mechanism and impact on the european climate in winter. *Physical Oceanography*. Retrieved from https://api.semanticscholar.org/CorpusID:133433424

Muilwijk, M., Ilicak, M., Cornish, S. B., Danilov, S., Gelderloos, R., Gerdes, R., ... Wang, Q. (2019). Arctic ocean response to greenland sea wind anomalies in a suite of model simulations. *Journal of Geophysical Research: Oceans*, *124*(8), 6286-6322. Retrieved from https://agupubs.onlinelibrary.wiley.com/doi/abs/10.1029/2019JC015101 doi: https://doi.org/10.1029/2019JC015101

Onarheim, I. H., Eldevik, T., Årthun, M., Ingvaldsen, R. B., & Smedsrud, L. H. (2015). Skillful prediction of barents sea ice cover. *Geophysical Research Letters*, *66*, 5364-5371. Retrieved from https://agupubs.onlinelibrary.wiley.com/doi/10.1002/2015GL064359 doi: 10.1002/2015GL064359

Oord, A., Dieleman, S., Zen, H., Simonyan, K., Vinyals, O., Graves, A., ... Kavukcuoglu, K. (2016). Wavenet: A generative model for raw audio. *arXiv preprint arXiv:1609.03499*. doi: https://doi.org/10.48550/arXiv.1609.03499

Polyakov, I. V., Ingvaldsen, R. B., Pnyushkov, A. V., Bhatt, U. S., Francis, J. A., Janout, M., ... ystein Skagseth (2023). Fluctuating atlantic inflows modulate arctic atlantification. *Science*, *381*(6661), 972-979. Retrieved from https://www.science.org/doi/abs/10.1126/science.adh5158 doi: 10.1126/science.adh5158

Rajabi-Kiasari, S., Delpeche-Ellmann, N., & Ellmann, A. (2023). Forecasting of absolute dynamic topography using deep learning algorithm with application to the baltic sea. *Computers Geosciences*, *178*, 105406. Retrieved from https://www.sciencedirect.com/science/article/pii/S0098300423001103 doi: https://doi.org/10.1016/j.cageo.2023.105406

Sarynina, R. (1969). Conditions of origin of cold deep-sea waters in the bear island channel. In *Physical variability in the north atlantic.*

Schauer, U., Loeng, H., Rudels, B., Ozhigin, V. K., & Dieck, W. (2002). Atlantic water flow through the barents and kara seas. *Deep-Sea Research Part I*, *49*(12), 2281-2298. Retrieved from https://doi.org/10.1016/S0967-0637(02)00125-5 doi: 10.1016/S0967-0637(02)00125-5

Sharma, S., Sharma, S., & Athaiya, A. (2017). Activation functions in neural networks. *Towards Data Sci*, *6*(12), 310–316.

Skagseth, Ø. (2008). Recirculation of atlantic water in the western barents sea. *Geophysical Research Letters*, *35*(11). Retrieved from https://doi.org/10.1029/2008GL033785 doi: 10.1029/2008GL033785

Skagseth, Ø., Drinkwater, K. F., & Terrile, E. (2011). Wind- and buoyancy-induced transport of the Norwegian coastal current in the barents sea. *Journal of Geophysical Research: Oceans*, *116*(C8), n/a–n/a. Retrieved from http://dx.doi.org/10.1029/2011JC006996 (C08007) doi: 10.1029/2011JC006996

Smedsrud, L. H., Esau, I., Ingvaldsen, R. B., Eldevik, T., Haugan, P. M., Li, C., ... Sorokina, S. A. (2013). The role of the barents sea in the climate system. *Review of Geophysics*, *51*(3), 415-449. Retrieved from https://doi.org/10.1002/rog.20017 doi: 10.1002/rog.20017

Tao, Q., Sjolte, J., & Muscheler, R. (2023). Persistent model biases in the spatial variability of winter north atlantic atmospheric circulation. *Geophysical Research Letters*, *50*(23), e2023GL105231. Retrieved from https://agupubs.onlinelibrary.wiley.com/doi/abs/10.1029/2023GL105231 (e2023GL105231 2023GL105231) doi: https://doi.org/10.1029/2023GL105231

Thompson, D. W. J., & Wallace, J. M. (1998). The arctic oscillation signature in the wintertime geopotential height and temperature fields. *Geophysical Research Letters*, *25*(9), 1297-1300. Retrieved from https://

agupubs.onlinelibrary.wiley.com/doi/abs/10.1029/98GL00950 doi: https://doi.org/10.1029/98GL00950

Wang, S., Sankaran, S., & Perdikaris, P. (2022). Respecting causality is all you need for training physics-informed neural networks. Retrieved from http://arxiv.org/pdf/2203.07404

Watanabe, E., Wang, J., Sumi, A., & Hasumi, H. (2006). Arctic dipole anomaly and its contribution to sea ice export from the arctic ocean in the 20th century. *Geophysical Research Letters*, *33*(23). Retrieved from https://agupubs.onlinelibrary.wiley.com/doi/abs/10.1029/2006GL028112 doi: https://doi.org/10.1029/2006GL028112

Willebrand, J., Philander, S. G. H., & Pacanowski, R. C. (1980). The oceanic response to large-scale atmospheric disturbances. *Journal of Physical Oceanography*, *10*(3), 411 - 429. Retrieved from https://journals.ametsoc.org/view/journals/phoc/10/3/1520-0485_1980_010_0411_tortls_2_0_co_2.xml doi: https://doi.org/10.1175/1520-0485(1980)010⟨0411:TORTLS⟩2.0.CO;2

Wu, B., Wang, J., & Walsh, J. E. (2006). Dipole anomaly in the winter arctic atmosphere and its association with sea ice motion. *Journal of Climate*, *19*(2), 210 - 225. Retrieved from https://journals.ametsoc.org/view/journals/clim/19/2/jcli3619.1.xml doi: 10.1175/JCLI3619.1

Yang, X.-Y., Yuan, X., & Tang, M. (2016). Dynamical link between the barents-kara sea ice and the arctic oscillation. *Journal of Climate*, *29*, 5103-5122. doi: 10.1175/JCLI-D-15-0669.1

Yi, K., Zhang, Q., Fan, W., Wang, S., Wang, P., He, H., . . . Niu, Z. (2024). Frequency-domain mlps are more effective learners in time series forecasting. *Advances in Neural Information Processing Systems*, *36*.